



A predator–prey model for moon-triggered clumping in Saturn's rings

Larry W. Esposito^{a,*}, Nicole Albers^{a,1}, Bonnie K. Meinke^{a,1}, Miodrag Sremčević^{a,1},
Prasanna Madhusudhanan^a, Joshua E. Colwell^{b,2}, Richard G. Jerousek^{b,2}

^a Laboratory for Atmospheric and Space Physics, University of Colorado, 392 UCB, Boulder, CO 80309, United States

^b Department of Physics, University of Central Florida, Orlando, FL 32816, United States

ARTICLE INFO

Article history:

Received 2 October 2009

Revised 22 June 2011

Accepted 28 September 2011

Available online 17 October 2011

Keywords:

Accretion

Occultations

Saturn, Rings

Ultraviolet observations

ABSTRACT

UVIS occultation data show clumping in Saturn's F ring and at the B ring outer edge, indicating aggregation and disaggregation at these locations that are perturbed by Prometheus and by Mimas. The inferred timescales range from hours to months. Occultation profiles of the edge show wide variability, indicating perturbations by local mass aggregations. Structure near the B ring edge is seen in power spectral analysis at scales 200–2000 m. Similar structure is also seen at the strongest density waves, with significance increasing with resonance strength. For the B ring outer edge, the strongest structure is seen at longitudes 90° and 270° relative to Mimas. This indicates a direct relation between the moon and the ring clumping. We propose that the collective behavior of the ring particles resembles a predator–prey system: the mean aggregate size is the prey, which feeds the velocity dispersion; conversely, increasing dispersion breaks up the aggregates. Moons may trigger clumping by streamline crowding, which reduces the relative velocity, leading to more aggregation and more clumping. Disaggregation may follow from disruptive collisions or tidal shedding as the clumps stir the relative velocity. For realistic values of the parameters this yields a limit cycle behavior, as for the ecology of foxes and hares or the “boom–bust” economic cycle. Solving for the long-term behavior of this forced system gives a periodic response at the perturbing frequency, with a phase lag roughly consistent with the UVIS occultation measurements. We conclude that the agitation by the moons in the F ring and at the B ring outer edge drives aggregation and disaggregation in the forcing frame. This agitation of the ring material may also allow fortuitous formation of solid objects from the temporary clumps, via stochastic processes like compaction, adhesion, sintering or reorganization that drives the denser parts of the aggregate to the center or ejects the lighter elements. Any of these more persistent objects would then orbit at the Kepler rate. We would also expect the formation of clumps and some more permanent objects at the other perturbed regions in the rings... including satellite resonances, shepherded ring edges, and near embedded objects like Pan and Daphnis (where the aggregation/disaggregation cycles are forced similar to Prometheus forcing of the F ring).

© 2011 Elsevier Inc. All rights reserved.

1. Introduction

Saturn's rings lie in the Roche zone surrounding Saturn, where the planet's tidal force and collisions limit accretion (Davis et al., 1984; Weidenschilling et al., 1984; Canup and Esposito, 1995; Barbara and Esposito, 2002; Karjalainen and Salo, 2004). Cassini observations can provide comparisons to processes in planet-forming disks (see recent reviews by Cuzzi et al. (2010) and Esposito (2010)). A particularly good region to observe the effects of

accretion is Saturn's F ring (Lane et al., 1982; Showalter and Burns, 1982; Esposito et al., 2008; Murray et al., 2005, 2008; Beurle et al., 2010). Other locations also give indications of particle clumping that may lead to accretion: straw-like features in the strongest density waves (Porco et al., 2005); elongated moonlets (Charnoz et al., 2007) embedded among the rings; objects causing propeller features in Saturn's A ring (Tiscareno et al., 2006, 2008; Sremčević et al., 2007) and embedded objects detected at equinox (Spitale and Porco, 2010). The presence of self-gravity wakes (Colwell et al., 2006, 2007; Hedman et al., 2007; Nicholson and Hedman, 2009) shows that the ring particles have a tendency to aggregate into trailing spiral structures throughout the rings. Ring simulations by Lewis and Stewart (2005, 2009) show the formation of temporary aggregations followed by disaggregation. This is especially evident if somewhat larger objects are included in their calculations. These “seeds” first collect, and then shed the smaller particles, which is supported by the observed shapes of the small

* Corresponding author. Fax: +1 303 492 1132.

E-mail addresses: larry.esposito@lasp.colorado.edu (L.W. Esposito), nicole.albers@lasp.colorado.edu (N. Albers), bonnie.meinke@lasp.colorado.edu (B.K. Meinke), miodrag.sremcevic@lasp.colorado.edu (M. Sremčević), Prasanna.madhusudhanan@colorado.edu (P. Madhusudhanan), jcolwell@physics.ucf.edu (J.E. Colwell), rjerousek@gmail.com (R.G. Jerousek).

¹ Fax: +1 303 492 6946.

² Fax: +1 407 823 5112.

moons near the rings (Porco et al., 2007). Barbara and Esposito (2002) suggested that the size distribution in Saturn's F ring is the outcome of a balance between the competing processes of fragmentation and accretion there.

In this paper, we show evidence of clumps forming in the rings at locations strongly perturbed by nearby moons with lifetimes from hours to months. We term this process “aggregation” which we use to include temporary structures. We reserve the term “accretion” to imply particles that stick together more permanently. The observed behavior can be explained by a simple “predator–prey” model of ring dynamics. If these aggregates that form from the satellite perturbations can even occasionally stick together to make gravitationally stable objects, those will persist, which is a possible explanation of the objects observed at Saturn equinox by Spitale and Porco (2010).

2. Occultations

The highest resolution studies of Saturn's rings are provided by star occultations (Esposito et al., 1998, 2004, 2005). Time resolution of UVIS occultations are 1–2 ms, providing diffraction-limited spatial resolution of meters to tens of meters in the ring plane. Multiple occultations can provide a 3D picture of the rings that resembles a medical “CAT” scan (e.g., Colwell et al., 2007). Spectral analysis of the time series of ring measurements also gives three-dimensional information, although this analysis does not resolve the individual features (Sremčević et al., 2008, 2009). The general dimensions, shape and alignment of ring structures can be derived from the auto-covariance of the occultation signal (e.g., Showalter and Nicholson, 1990). We describe in detail below the inferences about aggregation and its causes that may be drawn from evidence for particle clumping in the UVIS data set. UVIS has observed more than 100 stellar occultations by Saturn's rings. In this paper, we consider indications for clumping in the locations, optical depth, and sharpness of ring edges; location of the F ring core and the B ring outer edge; statistically significant features in Saturn's F ring; and sub-km structure seen by wavelet analysis.

3. Features in the F ring

Esposito et al. (2008) identified 13 statistically significant features in the first UVIS occultations. Esposito et al. interpreted these as temporary clumps and a possible moonlet, “Mittens”, which is totally opaque and has sharp edges in the occultation profile. At least one of the features, nicknamed “Pywacket”, was simultaneously observed by a VIMS occultation. Comparing the double star results for Pywacket, Esposito et al. concluded that it was likely elongated. The sharp edges indicate it is also significantly flattened. Meinke et al. (2011) now catalog and classify 27 features found in the first 101 stellar occultations by the F ring. Two features are opaque and candidates for solid objects: Mittens and a new feature, Sylvester. Both can be matched as a solid object surrounded by a skirt of loose material (Meinke et al., 2011).

The 17 features that represent aggregations, classified as “icicles” and “moonlets” by Meinke et al., show significant variation based on their location relative to Prometheus. All features are plotted versus Prometheus-relative longitude in Fig. 1, along with the quadrant average optical depth, indicated with its standard deviation. Both the number and optical depth are enhanced at the point opposite Prometheus. Of 17 features, nine have longitude relative to Prometheus of $\Delta\lambda = 189 \pm 20^\circ$. The maximum feature optical depth is found at $\Delta\lambda = 161^\circ$. A sinusoidal fit gives $\Delta\lambda = 191^\circ$, but with Pearson correlation only $r^2 = 0.1$. With r^2 so low, there is a significant probability ($p = 0.25$, Bevington, 1969) that this correlation could occur purely by chance. We note that

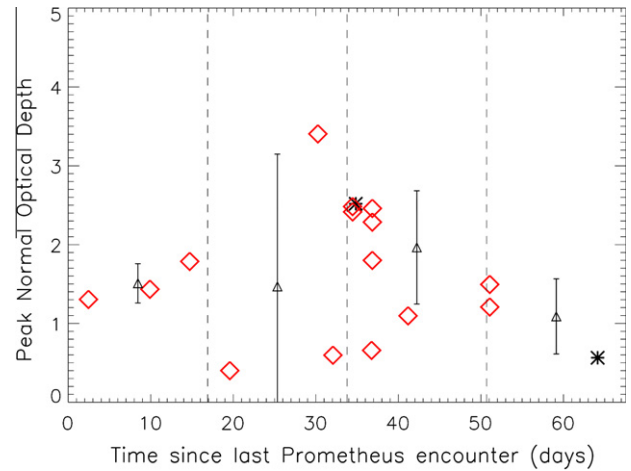


Fig. 1. Optical depth of icicles and moonlets (Meinke et al., 2011) versus the time since the feature last encountered Prometheus. The synodic period (~ 68 days) is divided into quadrants and the mean of optical depth for each quadrant is denoted by triangles with standard deviations. Stars: moonlets. Diamonds: icicles. The measured peak optical depth is plotted. The time on the ordinate shows one complete synodic period.

Hedman et al. (2011), using a different method to detect clumps in the F ring, find no significant correlation with Prometheus longitude. This disagreement with our result shows the F ring features correlation with Prometheus should be treated with caution. Even if the result we propose here is real, then other phenomena like the eccentric Prometheus orbit which brings it repeatedly close to the F ring may also contribute to observable structures (Beurle et al., 2010).

4. B ring edge thickness and sharpness

We applied the model of Jerousek et al. (2011) to the UVIS stellar occultation profiles of the B ring edge. This model parameterizes the radial and vertical variations in particle spatial number density with logistic (sigmoid) and gaussian functions, respectively. The thickness of the ring is only weakly constrained, but, the resolved edge profiles are sensitive to the radial parameter δ in the logistic function used to model the edge sharpness:

$$\tau(r) = \tau_{\max} \left[1 + \exp\left(\frac{r - r_{\text{edge}}}{\delta}\right) \right]^{-1} \quad (1)$$

where $r - r_{\text{edge}}$ is the radial separation between the occultation point and the edge. They find that roughly three-quarters of the profiles of the Huygens and Titan ringlet edges were well-described by this smooth, symmetric edge model. However, for the 64 high-signal-to-noise occultation profiles of the B ring edge we studied here, 48 exhibit complex structure within a few 100 m of the edge. Examples of the B ring edge with the best-fit model are shown in Figs. 3 and 4.

Even in the case of the complex edges, the parameter δ can be determined from the measurements describing the first transition from the Huygens gap to the B ring levels. In addition, we calculate an independent measure of the edge radial transition length, η , for those occultation where the light curve is completely insensitive to the ring thickness. This occurs, for example, in occultations at very high elevation angle above the ring plane, but also when the line of sight is nearly tangent to the edge. For these occultations, η is a direct measure of the radial distance over which the ring transitions from its full optical depth to the gap. This is related to δ , but η is larger than δ because η measures the full distance across the edge transition while δ is an e-folding length (Eq. (1)). Values for δ and η

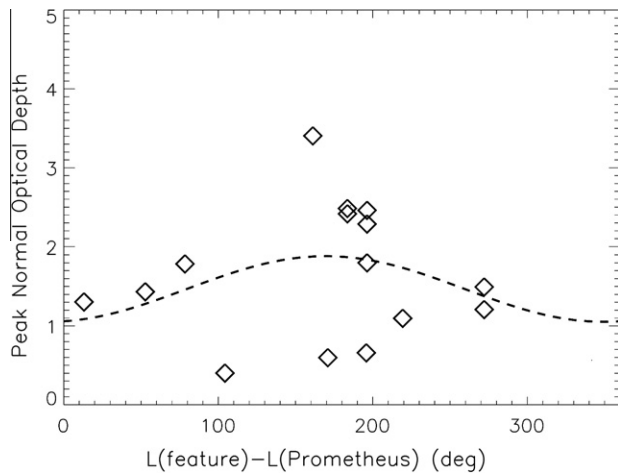


Fig. 2. Optical depth of icicles as a function of their separation in longitude from Prometheus. Icicles are those reported in Meinke et al. (2011). Dashed line is the sinusoidal fit of optical depth as a function of longitudinal separation from Prometheus. The fit gives a maximum optical depth at 191° separation from Prometheus.

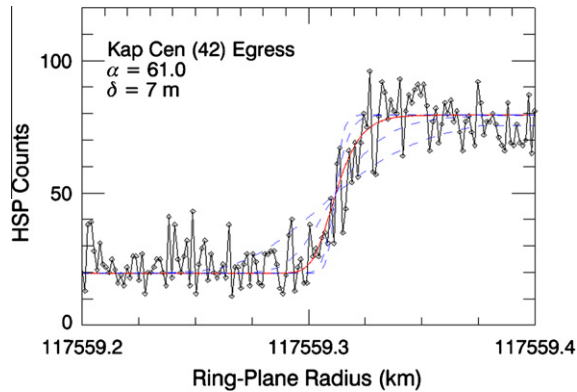


Fig. 3. A “symmetric” edge that is well-described by the model of Jerousek et al. (2011) from the Kappa Centauri (rev 42) egress occultation. The best fit model profile is shown in red, while the blue dashed curves are for values of the edge sharpness parameter δ that are 2 and 4 times larger and smaller than the best fit. The radial sampling for this occultation is 1.3 m.

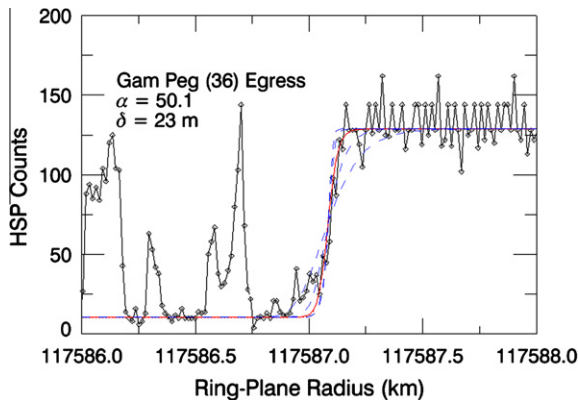


Fig. 4. An example of a complex edge profile from the γ Pegasi (rev 36) egress occultation. The sigmoid edge model fits the edge transition well, and the ring shows alternating opaque and transparent regions across the outermost kilometer. The radial resolution is 14 m, and the best fit value of δ (corresponding to the smooth model curve) is 9.2 m.

are shown in Fig. 5 as a function of longitude relative to Mimas and in Fig. 6 as a function of the absolute position of the edge, which is a proxy for the overall edge pattern. Neither shows a correlation between edge sharpness and Mimas or the edge position.

Although the derived parameters are not correlated with Mimas longitude, they indicate significant perturbations at very short spatial scales consistent with temporary aggregations, clumps or solid objects formed near the B ring edge.

5. B ring edge profiles and location

UVIS occultations show that the outer edge of the B ring is highly variable in location, morphology and optical depth. Much, but not all of the variability in location can be described using the multi-mode model by Spitale and Porco (2010). Albers et al. (2011) using HST and Cassini VIMS, RSS and UVIS data find post-fit RMS residuals of 9.6 km with a χ^2/DOF of ~ 100 , in agreement with the reported 10.1 km using HST and Cassini VIMS and RSS data (Hedman et al., 2010). This effectively leads to a slow beating where the resulting pattern amplitude takes a minimum in 2006–2007 (Fig. 7). Notably, the minimum of a simple $m = 2$ pattern is leading Mimas by 45° in 2004–2005 (upper panel in Fig. 7) while trailing Mimas by 25° in 2008–2009 (lower panel in Fig. 7). This is similar to the findings of Hedman et al. (2010) who report that the B ring edge is leading in 2005 and lagging in 2008 by 35° and 20°, respectively.

Edge profiles exhibit multiple shapes ranging from plateaus, steep hillsides, broad hummocks, to ragged regions. Albers et al. (2011 and work to be published) show that many but not all of these can be explained by greater compression of the particle streamlines where the highest optical depths are measured when the edge is inward of the radial location of the Mimas 2:1 Inner Lindblad Resonance (ILR).

Occultations since 2005 show both the measured values of optical depth and their variance increasing (Fig. 8). Employing Levene's test (Brown and Forsythe, 1974) we confirm this trend with 76% confidence when excluding observations where the edge appears opaque and only a lower limit for the true optical depth is inferred. (Including all available observations yields a confidence level of 94%.) This is further supported by the increase over time in the significance of sub-km structure evident in the wavelet spectral analysis (see below). Also, maxima in the optical depths are seen when the data are plotted relative to Mimas's location, at 0° and 180° relative to the moon. It is significant that these same longitudes are minima in the significance of the sub-km structure.

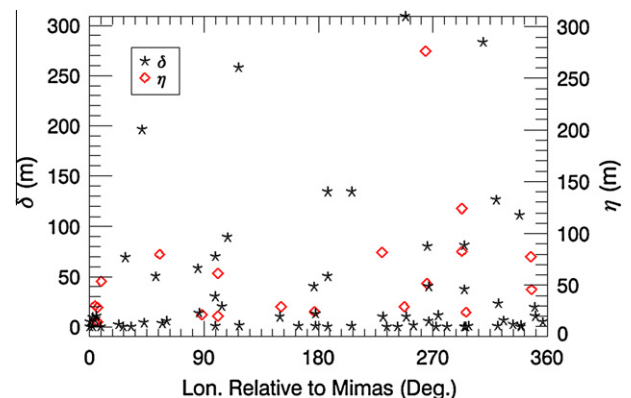


Fig. 5. Edge sharpness as measured by the logistic function parameter δ (asterisks, Eq. (1)) and as measured directly from the radial extent of the transition in the light curve (diamonds, η) in a frame corotating with Mimas.

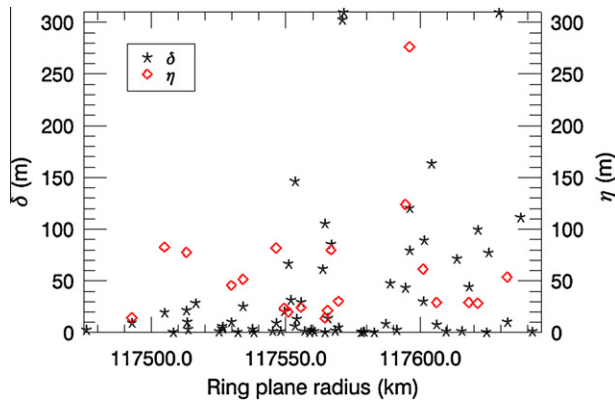


Fig. 6. Edge sharpness as measured by the logistic function parameter δ (asterisks, Eq. (1)) and as measured directly from the radial extent of the transition in the light curve (diamonds, η) as a function of the position of the edge.

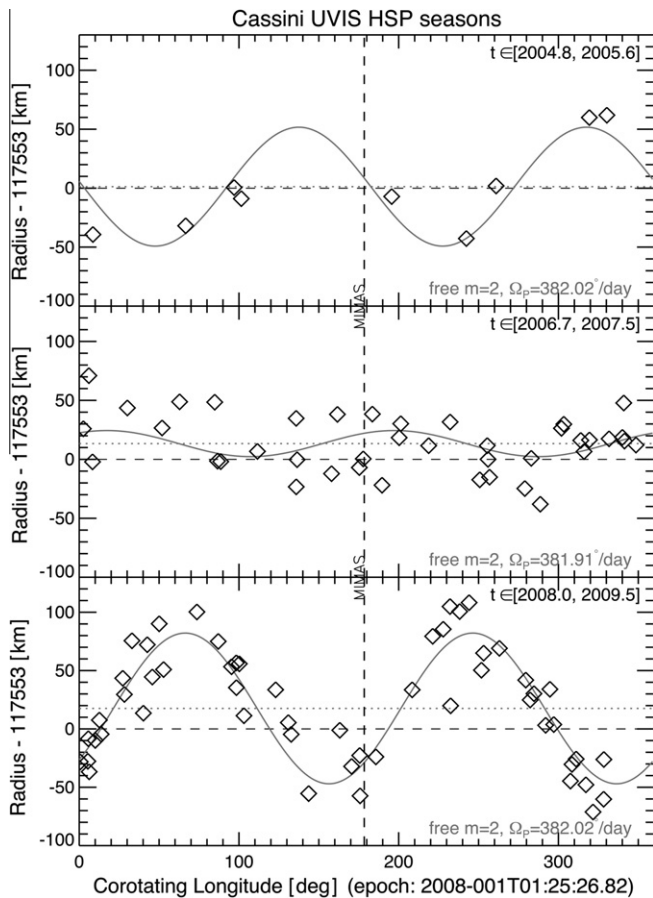


Fig. 7. B ring edge as seen in three occultation seasons. Grey lines denote best fit $m=2$ pattern for the corresponding subset time interval given in years for each panel. Each data subset is precessed to common epoch 2008 – 001T01:25:26.8. Mimas' relative position is marked (dashed line). The pattern amplitude has a minimum in the period 2006–2008 (middle panel).

6. F ring core

Unlike the F ring features (Meinke et al., 2009) discussed above (Figs. 1 and 2), the F ring core optical depth exhibits no obvious secular trend related to Prometheus. Its position is well-described by a freely precessing ellipse, with typical residuals less than 50 km (Albers et al., 2009). Using a periodogram analysis (Scargle, 1982), Albers et al. (2011) confirm a trace of the expected Prome-

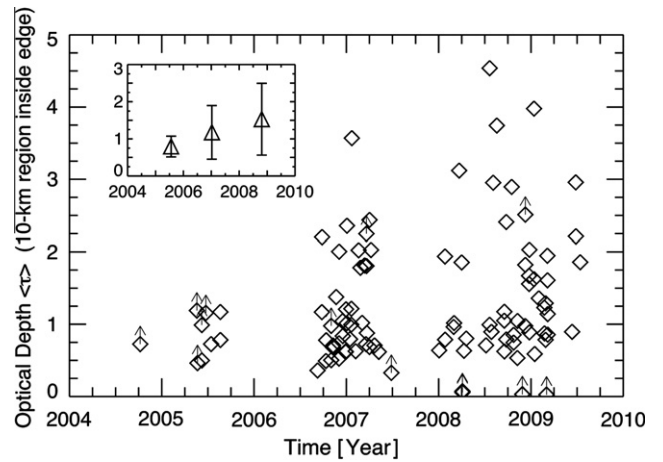


Fig. 8. Optical depth of outer edge of B ring over time. The plotted values are the mean of the 10-km region inside the observed edge. Arrows show lower limits, where the transmitted star brightness was not distinguishable from zero. Insert: Means with standard deviations for these occultation seasons. The B ring edge shows both azimuthal and significant temporal variability in optical depth.

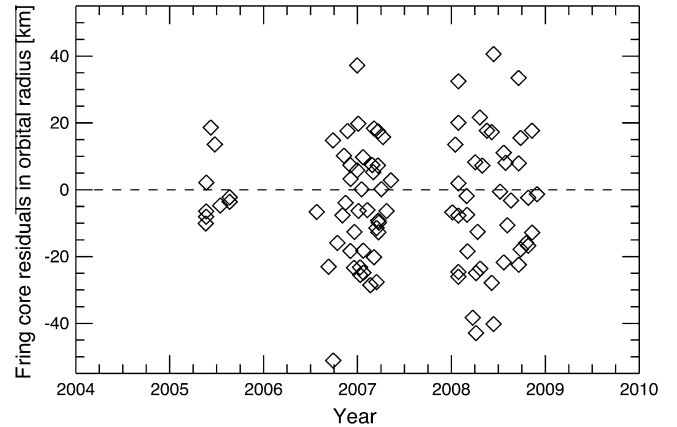


Fig. 9. F ring core perturbed by Prometheus. Residuals are in orbital radius relative to the orbit model in Albers et al. (2009). The variance of the F ring core residuals is increasing, coincident with the upcoming anti-apse alignment of Prometheus and ring in December 2009.

theus signature with a period of about 3.2° (e.g., Kolvoord et al., 1990) in optical depth (60% confidence) but find the residuals to have a slightly larger period 3.5° (91% confidence). This is evidence of the strong dynamical interaction of moon and ring. Moreover, the variance of the F ring core residuals increases with time (Fig. 9), presumably as the F ring and Prometheus neared their apse anti-alignment in December 2009. The RMS of the residuals of about 23 km is comparable to the estimated change in radius of about 18 km, using the predicted changes in eccentricity of 13×10^{-5} at anti-alignment (Murray et al., 2008).

7. Sub-km structure seen by wavelet analysis

To quantify small scale structure seen by the UVIS occultation, we calculate the weighted wavelet Z-transform (WWZ) Foster (1996). This variate (in the following text and plots we label it as statistical significance) follows the F -distribution with $N_{\text{eff}}=3$ and 2 degrees of freedom (see Foster, 1996, Eqs. (5)–(12)). Here N_{eff} is effective number of data points, and the distribution has expectation value unity, $F=1$. An F value greater than 3.0 for a large number of data points and 2 degrees of freedom corresponds to a

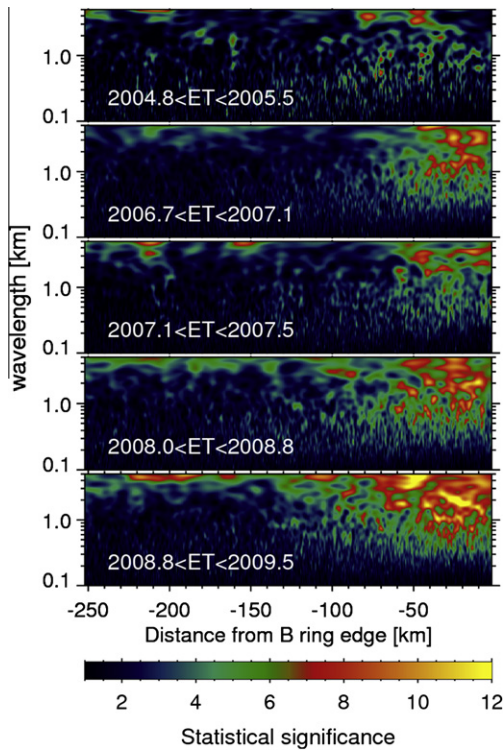


Fig. 10. Average significance of wavelet power (weighted Z – transform, summed over multiple occultations, see text, for successive subsets of occultation data. The area shows 250 km inside the B ring edge. Each frame presents the mean from all occultations within the time period indicated, for wavelength scales of 0.1 to 5 km. The statistical significance, as calculated using Foster (1996) WWZ wavelet toolkit, is indicated by color bar at bottom. The top-most panel is based on only five occultations, which were by rather dim stars or with low B angle and the significance is questionable. In contrast other panels are based on 23, 15, 21 and 25 occultations, respectively. Any subset of occultations cover essentially random corotating longitudes, which is clear from Fig. 7. The wavelet cone-of-influence is outside the figure and does not affect the shown values.

probability of less than 5% of occurring by chance. For 99% confidence, the corresponding F value is 4.6. (Bevington, 1969, Tables C-6 and C-7). This provides a natural choice for summing the power spectral data from multiple occultations with different star brightness, elevation angle B , background and radial resolution. We additionally resample high-resolution occultations to about 10 m in order to maintain a similar value of N_{eff} from the different occultations. We therefore sum the results of this wavelet analysis (Foster, 1996) of the occultation data to identify significant events. By converting the results of each occultation to statistical significance (that is, to a variate whose distribution corresponds to the F distribution) the summed results give an average value of the significance of features in the power spectrum detected by the wavelet algorithm.

It is already known that the power in the wave structure, with characteristic radial scales of tens of km, allows easy detection of density waves (Tiscareno et al., 2007; Colwell et al., 2009a). The Foster (1996) wavelet toolkit and coadding of the spectral information have been successfully applied to detect density waves and quantify details of their non-linear dispersion (Sremčević et al., 2008), to analyze weak Cassini division density waves (Colwell et al., 2009b) to detect new waves in the C ring (Baillié et al., 2011), and to infer properties of overstable wavelengths within the A and B rings (Sremčević et al., 2009). The spatial resolution of the UVIS occultations allows us to search for structure at radial scales much smaller than the wavelengths of density waves. We report here such structure at the B ring edge and in the strongest

density wave trains, which has significant amplitude at radial scales from 200 to 2000 m. We interpret the significant values not as periodic phenomena, but as structures with the characteristic wavelength of the Morlet wavelet. We call this finer structure evident in the wavelet analysis “sub-km structure”.

For the B ring outer edge, the significance of features with sizes 200–2000 m has been generally increasing since 2004, and is now at its highest value during the Cassini mission (Fig. 10). When we sort our occultations by longitude relative to Mimas, the binned data clearly show the maximum structure at 90° and 270° ahead of Mimas, (Fig. 11). These longitudes follow the 2:1 Mimas compression that occurred a few hours earlier, consistent with the expectation from simulations that clumps form somewhat after the moment of maximum compression of the particle streamlines (Lewis and Stewart, 2005). This is clear evidence for clumping triggered by the moon Mimas, followed by disaggregation in the next quadrant with a timescale of merely hours.

We see similar sub-km structure using a similar analysis at the locations of the strongest density waves (Fig. 12). We have checked all the strongest resonances from Lissauer and Cuzzi (1982). This observed power may be due to smaller structures below the spatial resolution of ISS or perhaps to pre-cursors of the phenomena called “straw” by Porco et al. (2005). The connection to the moon forcing is obvious: we see such structure only at the strongest density waves, and its significance is directly correlated to the resonance torque (Fig. 13).

8. Summary of observational findings

At perturbed locations in the rings, we directly observe moon-induced structures. Dynamical perturbations manifest themselves in anticipated and regular patterns such as the F ring core orbit perturbations by Prometheus or the underlying $m = 2$ pattern of the B ring edge in response to Mimas. Additionally, we find evidence for the response of the ring on the scale of individual particles and clumps. (1) The B ring edge is more variable than other edges. (2) Sub-km structure is correlated with torque for density waves and longitude for the B ring edge, and anti-correlated with optically thick regions. These correlations indicate that the moon is responsible for these visible manifestations of ongoing clumping in the rings. We see the ring response increase and then decrease on a time scale comparable to the synodic period of moon forcing. This is an indication of competing, possibly cyclic processes, which show that we are not observing a simple instability to growth of small objects into larger aggregates.

The combination of events triggered by moons and seeded by existing aggregates or solid cores could explain some part of the temporal variations seen in the B ring edge. The largest of such hypothetical objects indicted by UVIS data (with dimensions of several km) are large enough to be visible to ISS (Spitale and Porco, 2010). However, the clumps that we measure are not the equinox objects they see. Those seen by ISS are persistent over many years, are seen in two regions that Spitale and Porco call “A” and “B”, and orbit at the Kepler rate. Below, we speculate that rare events may cause the temporary clumps UVIS detects to become solid objects. Then, they would orbit at the Kepler rate, and have longitudes independent of the forcing moon, as observed by Spitale and Porco, 2010.

9. Predator–prey kinetic model for moon-perturbed rings

To better understand the temporary aggregations, we develop a simplified model that can address the long-term behavior of perturbed rings, as follows:

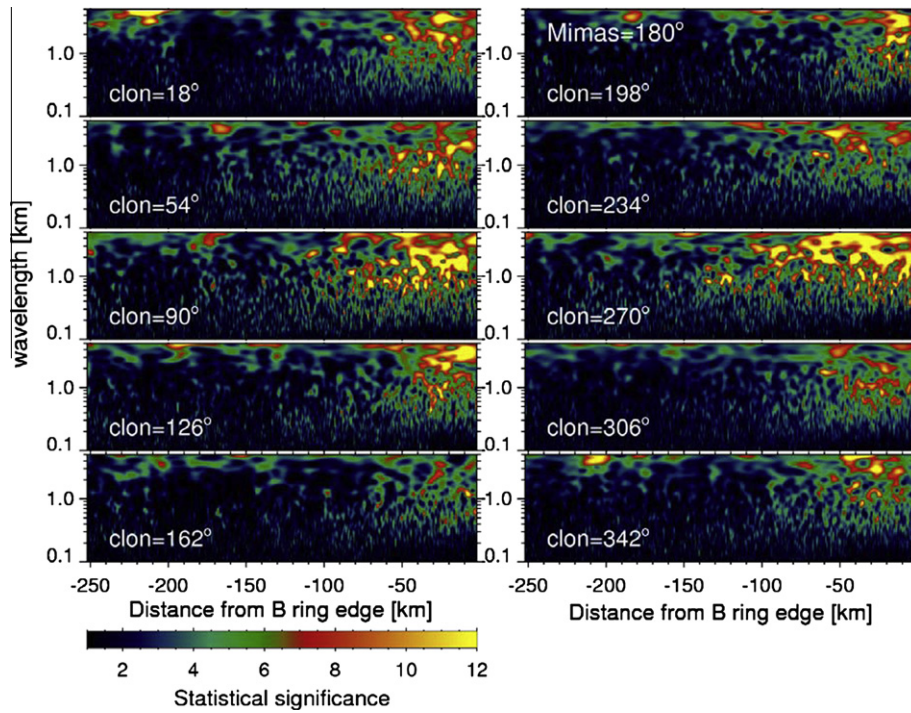


Fig. 11. Average significance of sub-km structure from wavelet analysis, as in Fig. 10. The area shows 250 km inside the B ring edge. Each frame represents the mean from all occultations in 36° bins of corotating longitude: $\text{clon} = \text{lon} - n * (t - t_0)$. Here lon is inertial longitude, n is the pattern speed which was chosen as the Mimas mean motion 381.9944522 deg/day. At the chosen epoch (t_0) of 2008–001T01:25:26.8, Mimas is located around 180° .

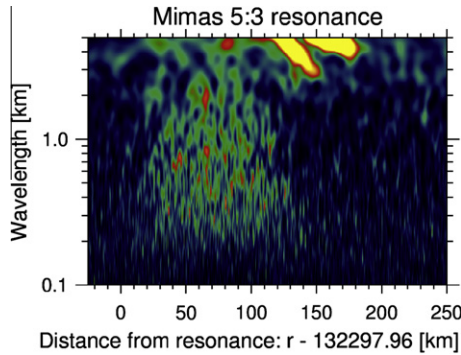


Fig. 12. Statistical significance calculated at the location of Mimas 5:3 inner Linblad resonance (ILR). The signature of the corresponding density wave is at larger wavelengths barely visible here (the tip of the density wave is seen near the distance of 130 km at the top). Data are averaged from all occultations. The color bar scale as in Figs. 10 and 11.

9.1. Kinetic equation

For a dilute granular ensemble like Saturn's rings, Spahn et al. (2004, Eq. (1)) self-consistently write the kinetic equation as

$$\frac{D}{Dt} F(\vec{m}, \vec{r}, \vec{v}, t) = \left. \frac{DF}{Dt} \right|^{(c)} + \left. \frac{DF}{Dt} \right|^{(f)} = G^{(c)} - L^{(c)} + G^{(f)} - L^{(f)} \quad (2)$$

where F is the generalized distribution function of a co-moving element of the ensemble at location \vec{r} . G and L are the gain and loss terms due to coagulation and fragmentation. The substantive derivative D/Dt accounts for all system dynamics except binary particle interactions.

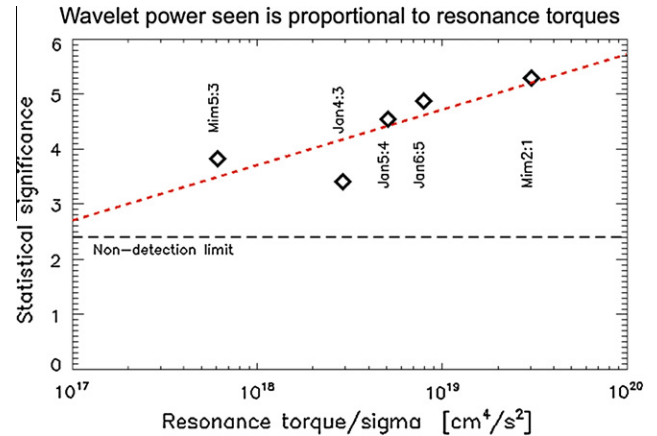


Fig. 13. Density wave sub-km structure is correlated with resonance strength. Values are mean significance for wavelengths between 0.2 km and 2 km and distance from resonance between 10 km and 90 km outside (cf. Fig. 13). In the case of Mimas 2:1 we repeated exactly the same procedure as for Figs. 12 and 13, except that statistical significance is taken from within 90 km interior to the B ring edge. Resonance torque is from Lissauer and Cuzzi (1982). Dashed line is the best linear fit, correlation $r = 0.81$. The non-detection limit of 2.4 is estimated from the nearby ring regions where no structure is detected (indicated by the dark-bluish background color in Figs. 10–12). (For interpretation of the references to color in this figure legend, the reader is referred to the web version of this article.)

9.2. Mass evolution

Blum (2006, Eqs. (4)–(7)) assumes isotropic binary collisions among the ensemble elements. Integrating over velocity and letting the substantial derivative transform to a partial derivative for a force-free system, he writes the terms for coagulation and fragmentation in terms of kernels K_a and K_f for each (a is for ‘agglomeration’). This gives explicit integrals for G and L from Eq.

(2). At a characteristic location \check{r} , he writes the coagulation equation (compare Spahn et al., 2004, Eq. (7))

$$\begin{aligned} \frac{\partial n(m, t)}{\partial t} = & \frac{1}{2} \int_0^m K_a(\bar{m}, m - \bar{m}) n(\bar{m}, t) n(m - \bar{m}, t) d\bar{m} \\ & - n(m, t) \int_0^\infty K_a(\bar{m}, m) n(\bar{m}, t) d\bar{m} + \frac{1}{2} \\ & = \int_0^\infty \int_0^\infty P(m, \bar{m}, m', v') K_f(\bar{m}, m) n(\bar{m}, t) n(m', t) d\bar{m} dm' \\ & - n(m, t) \int_0^\infty K_f(\bar{m}, m) n(\bar{m}, t) d\bar{m} \end{aligned} \quad (3)$$

Here, P represents the probability that collisions between \bar{m} and m' striking at relative velocity v' will produce fragments of size m . The terms on the right hand side represent coagulation gain, coagulation loss, fragmentation gain and fragmentation loss respectively.

9.3. Coagulation terms

The first two terms in Eq. (3), which are $G^{(c)}$ and $L^{(c)}$ from Eq. (2), can be re-written if we assume all aggregates are composed of monomers of mass m_0 . This is an extreme approximation but preserves the basic physics. Compare Spahn et al. (2004) Fig. 3 with Blum (2006) Fig. 3. For a variety of assumptions about the coagulation kernels K_a , this gives exponential growth with a timescale T_{coll}/α , where T_{coll} is the time between collisions and α is the sticking coefficient (Blum, 2006, Eqs. (23), (26), (35), (40), and (48)). Blum (2006, p. 893) notes that ‘smaller agglomerates always dominate in particle number over larger agglomerates, although the mean mass increases [with time]’.

We define the effective mass (e.g., Morishima et al., 2008)

$$M = \frac{\int_0^\infty m^2 n(m, t) dm}{\int_0^\infty m n(m, t) dm} \quad (4)$$

Blum (2006, Eq. (33)) calls this moment the ‘mean agglomerate mass’. This will be important in determining the velocity evolution of our system, below. Stewart and Wetherill (1988, Eqs. (7), (8a), and (9a)) show that the viscous stirring is proportional to the square of the mass of the larger aggregates; Morishima et al. (2008, Eqs. (11)–(15)) show that the velocity evolution is regulated by the larger bodies and that the mean eccentricity depends directly on this effective mass (their Eq. (15)). We therefore replace the coagulation terms in Eq. (3) by taking the moment (Eq. (4)) of the left hand side, and approximating the right hand side by the simple solution for monomers

$$\frac{dM}{dt} = \frac{M}{T_{\text{acc}}} \quad [\text{coagulation only}] \quad (5)$$

From Shu and Stewart (1985, after their Eq. (9)), we approximate the collision time for a power law distribution of particle sizes by

$$T_{\text{coll}} \approx \frac{T_{\text{orb}}}{4\tau} \quad (6)$$

where τ is the measured optical depth in the ensemble at location \check{r} , and T_{orb} is the orbital period.

9.4. Fragmentation terms

Blum (2006, pp. 929–931) notes that impact experiments with high porosity aggregates give a sticking threshold of about 1 m/s. Above this relative velocity, colliding particles preferentially fragment, eroding the larger aggregate. A steep transition between sticking and non-sticking is observed for many targets, including smooth solid targets, single projectile particles and fractal aggregates

(Blum, 2006). Where sticking does not occur, the target typically loses a mass similar to the projectile. Using similar level of approximation, as in Eq. (5), we re-write the fragmentation terms in Eq. (3) as

$$\frac{dM}{dt} = - \frac{v_{\text{rel}}^2}{v_{\text{th}}^2} \frac{M}{T_{\text{coll}}}, \quad [\text{fragmentation only}] \quad (7)$$

where $\left(\frac{v_{\text{rel}}^2}{v_{\text{th}}^2}\right)$ makes for a sharp transition, v_{rel}^2 is the velocity dispersion (see below) and v_{th} is the threshold velocity for sticking (Blum, 2006; Albers and Spahn, 2006). This formulation assumes that the aggregates are held only by adhesion. For larger aggregates, it might be more appropriate to use the escape velocity as the threshold, but we do not consider this possible improvement in this paper. These approximations (Eqs. (5) and (7)) combine to give the evolution for the mean aggregate mass

$$\frac{dM}{dt} = \frac{M}{T_{\text{acc}}} - \left(\frac{v_{\text{rel}}^2}{v_{\text{th}}^2}\right) \frac{M}{T_{\text{coll}}} \quad (8)$$

9.5. Velocity evolution

We define the mean random velocity in the co-moving group of ring particles in our ensemble

$$v_{\text{rel}}^2 = \int_0^\infty n(m) v_{\text{rel}}^2(m) dm \quad (9)$$

Schmidt et al. (2009, Eq. (14.11)) write the equation for evolution of the velocity dispersion, where the rate of change is given by the losses due to dissipation and the contributions of local and non-local viscous stirring. With a similar level of approximation as above, we re-write their equation as

$$\frac{dv_{\text{rel}}^2}{dt} = - \frac{v_{\text{rel}}^2(1 - \varepsilon^2)}{T_{\text{coll}}} + \nu S^2 \quad (10)$$

where ε is the normal coefficient of restitution, ν is the viscosity and S is the shear rate. The first term represents collisional dissipation and the second viscous stirring. Schmidt et al. (2009, p. 425) note ‘In the case of strong wakes the total viscosity is dominated by the angular momentum transfer related to the gravitational torques exerted by the inclined wakes’. Since we similarly believe the momentum transfer will be dominated by the local aggregates forming in moon-perturbed ring regions, we calculate the viscosity due to aggregates of mass M . They find (their Eq. (14.50))

$$\nu \approx C(r_h) \frac{G^2 \Sigma^2}{\Omega^3} \quad (11)$$

as was earlier discussed by Ward and Cameron (1978), without the correction factor from Daisaka et al. (2001). Assuming $C(r_h)$ is of order unity, we arrive at the second of our simplified equations

$$\frac{dv_{\text{rel}}^2}{dt} = - \frac{v_{\text{rel}}^2(1 - \varepsilon^2)}{T_{\text{coll}}} + \frac{M^2}{M_0^2} \frac{v_{\text{esc}}^2(M_0)}{T_{\text{orb}}} \quad (12)$$

where M_0 is a reference mass and v_{esc} is the escape velocity from its surface. This approximates the viscous stirring by the passage of a clump of mass M increasing the dispersion to its escape velocity on the time scale of one orbital period. This approximation will hold as long as the growth of aggregates does not significantly reduce the background surface mass density, which provides the raw material that the aggregate uses to grow. This is a good approximation in Saturn’s rings where the aggregates make up a small portion of the total ring mass.

Table 1

Parameters for predator–prey model runs.

Parameter	B ring edge	F ring	Notes
T_{orb}	1	1	Scale all times to T_{orb}
T_{coll}	$\tau = 1, 1.5$	$\tau = 0.1$	$T_{\text{orb}}/(4 * \tau)$
T_{acc}	"	"	$T_{\text{acc}} = T_{\text{coll}}$ since $\alpha = 1$
T_{diss}	$T_{\text{orb}}/3.84$	$T_{\text{orb}}/0.63$	Since $\varepsilon = 0.6$
M_0	$2 \times 10^9 \text{ g}$	$2 \times 10^9 \text{ g}$	10 m aggregate with internal density $\rho = 0.5 \text{ g/cm}^3$
T_{stir}	1, 2 T_{orb}	1, 4 T_{orb}	Stirring occurs roughly over one orbital period
V_{esc}	0.5 m/s	0.5 m/s	Escape velocity at surface of M_0
T_{syn}	0.5 T_{orb}	112 T_{orb}	Forcing period
A_0	0.1, 0.5, 0.9	0.1, 0.5, 0.9	$* 2 \pi * V_{\text{th}}^2 / T_{\text{syn}}$

9.6. Predator–prey model

We have simplified the kinetic description to two equations (Eqs. (8) and (12)):

$$\begin{aligned} \frac{dM}{dt} &= \frac{M}{T_{\text{acc}}} - \left(\frac{v_{\text{rel}}^2}{v_{\text{th}}^2} \right) \frac{M}{T_{\text{coll}}} \\ \frac{dv_{\text{rel}}^2}{dt} &= -\frac{v_{\text{rel}}^2(1 - \varepsilon^2)}{T_{\text{coll}}} + \frac{M^2}{M_0^2} \frac{v_{\text{esc}}^2(M_0)}{T_{\text{orb}}} \end{aligned} \quad (13)$$

These equations represent a simple model of the coupled evolution dynamics. A similar approach has been used to simplify the dynamics of zonal flows in a plasma (Diamond et al., 2005, Eqs. (2.9) and (2.10)) and in Earth's aerosol-cloud precipitation system (Koren and Feingold, 2011). This minimal system of two equations is similar to a 'predator–prey' model in ecology (e.g., May, 1974). The mean aggregate mass corresponds to the prey population; the velocity dispersion corresponds to the predators: it 'feeds' off the accelerations from the aggregates' gravity. If the velocity dispersion grows too large, it limits the prey: higher velocities fragment the aggregates. In the absence of interaction between mass and velocity, the prey (mean aggregate mass) grows and the

predator population (dispersion velocity) decays. When they interact, the ensemble reaches a stable equilibrium for size distribution and a corresponding thermal equilibrium (e.g., Stewart et al., 1984). Our approach includes accretional aggregate growth, collisional disruption, dissipation and viscous stirring. It differs from the approach of Showalter and Burns (1982): they follow the orbits of test particles without collisions. In our model, moons disturb the ensemble, not just the orbits. In Showalter and Burns (1982), the particles briefly congregate, but then shear on through to form a mostly uniform ring again.

The Eq. (13) are similar to the Lotka-Volterra equations for a predator–prey system. The differences are in the second term of the second equation. Instead of M we have M^2 ; instead of v_{rel}^2 , we have v_{esc}^2 . This system has a non-trivial fixed point, where we satisfy the criterion

$$\frac{dM}{dt} = \frac{dv_{\text{rel}}^2}{dt} = 0 \quad (14)$$

Near the fixed point, the level curves are ellipses, the same as for the pendulum. The size and shape of the level curves depends on the amplitude of any forcing: in the absence of forcing, the system decays to the stable fixed point, as expected, given the natural dissipation (see Stewart et al., 1984). As the system limit cycles, the predators lag the prey by $\pi/2$. In particular, the prey (mass) peaks 90° after the predator (velocity) minimum.

We have numerically solved the Eq. (13) with an added forcing term to describe the moon perturbation, which for simplicity, we assume to be periodic with the synodic period ω :

$$\begin{aligned} \frac{dM}{dt} &= \frac{M}{T_{\text{acc}}} - \left(\frac{v_{\text{rel}}^2}{v_{\text{th}}^2} \right) \frac{M}{T_{\text{coll}}} \\ \frac{dv_{\text{rel}}^2}{dt} &= -\frac{v_{\text{rel}}^2(1 - \varepsilon^2)}{T_{\text{coll}}} + \frac{M^2}{M_0^2} \frac{v_{\text{esc}}^2(M_0)}{T_{\text{orb}}} - A_0 \cos(\omega t) \end{aligned} \quad (15)$$

We find similar results for periodic impulsive forcing.

We present solutions to Eq. (15) for selected values of the parameters corresponding to the ring properties at the B ring outer edge (perturbed by the Mimas 2:1 ILR) and the F ring (perturbed by

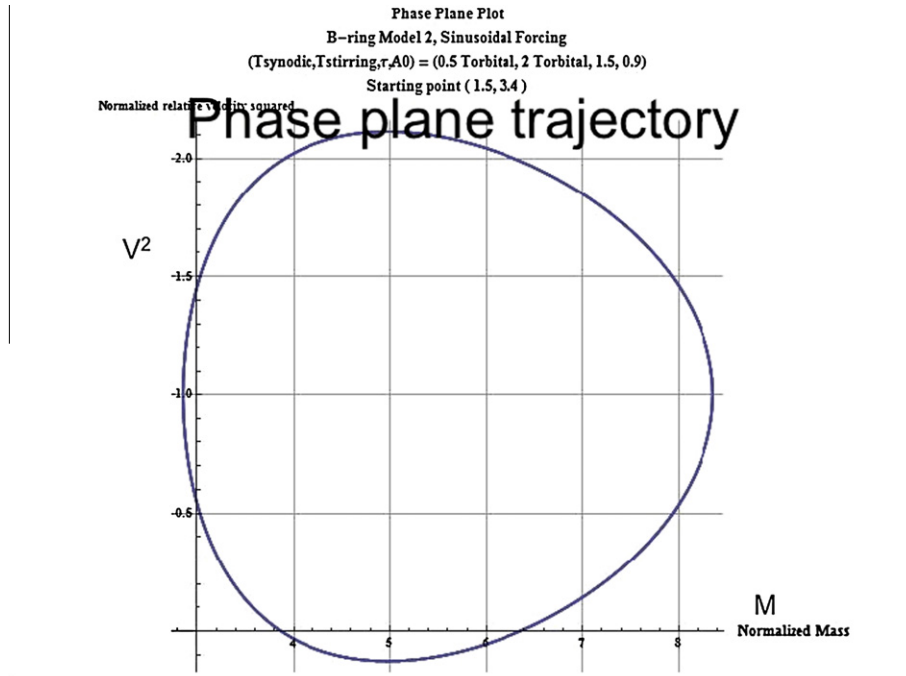


Fig. 14. Phase plane trajectory for predator–prey model for Saturn's B ring. Forcing period is half the orbital period. The viscous stirring timescale (τ_{stir}) is 2 orbital periods. Optical depth $\tau = 1.5$. Forcing amplitude $A_0 = 0.9$ (see Table 1). The system cycles counter-clockwise.

successive passes of Prometheus). See Table 1. In Fig. 14, we plot the phase plane trajectory for our system at the B ring edge. The limit cycle is not a perfect ellipse, as for the pure predator–prey model, but slightly flattened. Nonetheless, our system reproduces the major characteristics of an ecological system’s predator–prey balance. The system cycles about the fixed point, and the maxima are out of phase (Fig. 15). We find that the amplitude of the excursions around the fixed point is proportional to the forcing amplitude A_0 (Figs. 16 and 17). We believe this can explain the behavior shown in Fig. 13, that wavelet power (indicating temporary clumps described by the variable M in our model) is greater for greater forcing. Our simulations show, as expected, that the mass (prey) peaks $\pi/2$ after the velocity (predator) minimum (see Fig. 15).

9.7. Phase lag

Lewis and Stewart (2000, Fig. 5) show that for the Encke Gap edge perturbed by Pan, the forced eccentricity is mostly damped by about 1 radian downstream from the moon. In the wake peaks, the dispersion is reduced. They note that the close packing has forced all the ring particles to nearly identical trajectories, reducing the velocity dispersion. We believe a similar phenomenon will occur in Saturn’s F ring perturbed by Prometheus, leading to a dispersion minimum following the moon’s passage... and based on our simple model, causing aggregate growth followed by disaggregation downstream.

At the B ring edge, particle orbits are similarly perturbed by the Mimas 2:1 resonance. Streamlines will crowd, exciting a predator–prey cycle of aggregation/disaggregation. Since the transients will damp out, the long-term behavior expected is a driven pattern at the frequency of the Mimas forcing. For this steady state to arise, clumps must persist at least one synodic period. Cassini images of the F ring indicate that this is true (Beurle et al., 2010). This also

seems likely for the outer B ring, where the forcing period is only half an orbital period. Since the minimum separation of particle streamlines in the resonance will lag the Saturn–Mimas line (Murray and Dermott, 1999, p. 502) the dispersion minimum will also be located somewhat downstream of the Mimas longitude.

This model predicts that the maximum aggregate mass M lags the perturbing moon (F ring) or the resonance peak longitude (B ring edge). The observed peak should be the sum of the lag for the perturbation to reach velocity dispersion minimum and the lag of $\pi/2$ predicted by the predator–prey dynamics. This would be about 150° lagging to Prometheus and about 105° and 305° leading Mimas (since its streamlines crowd twice around) if the first lag is about 1 radian (60°) as shown in Lewis and Stewart (2000, Fig. 5). We believe these expectations are consistent with our somewhat noisy results. See our conclusions below.

9.8. Discussion

Our interpretation is that the moon flyby or density wave passage excites the forced eccentricity in the ring system. This causes the streamlines to crowd, as demonstrated by Lewis and Stewart (2000, 2005). The relative velocity is damped there. If the density enhancement also increases the gravitational attraction, the effect could be even larger. This is not considered in our model, but evidence for such effects are seen in the observations reported by Beurle et al. (2010).

The moon drives the collective aggregation/disaggregation of the system (15) at a frequency that is below its natural limit cycle frequency. The impulse creates crowding, which damps the velocity, which in turn enhances growth until the aggregate viscous stirring excites velocities high enough to erode and fragment the aggregates. The effects of this individual impulse would eventually damp, but successive forcing at the driving frequency yields a steady state response at a frequency ω in this driven system (Landau

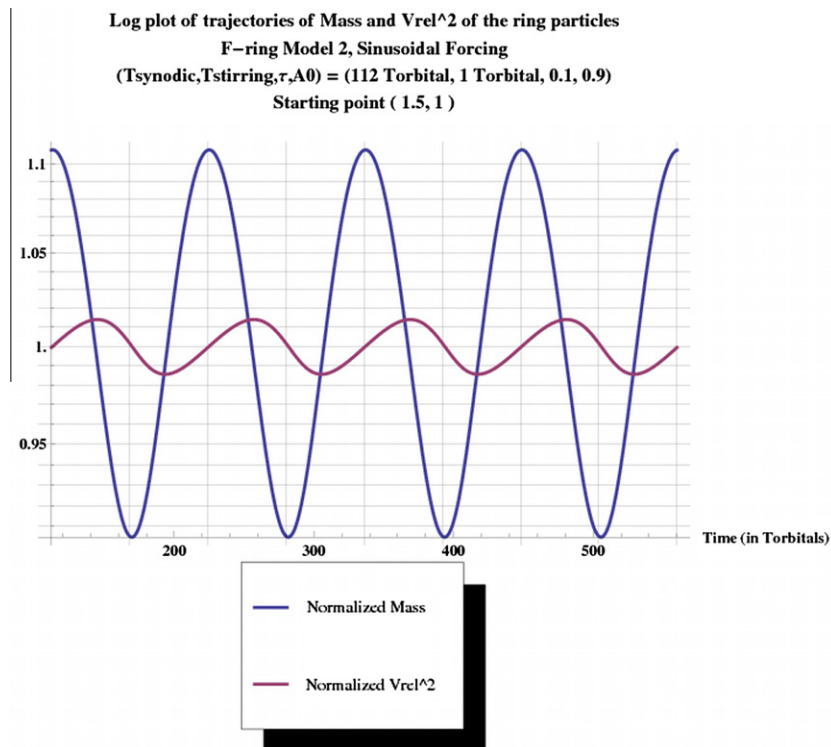


Fig. 15. Time dependencies of mass and v_{rel}^2 for predator–prey model for Saturn’s F ring. Sinusoidal forcing at the synodic period of Prometheus (112 orbits). The viscous stirring timescale (τ_{stir}) is one orbital period. Optical depth $\tau = 0.1$. Forcing amplitude $A_0 = 0.9$ (see Table 1). In the steady-state (shown) the mass peak lags the velocity minimum by a quarter period, $\pi/2$.

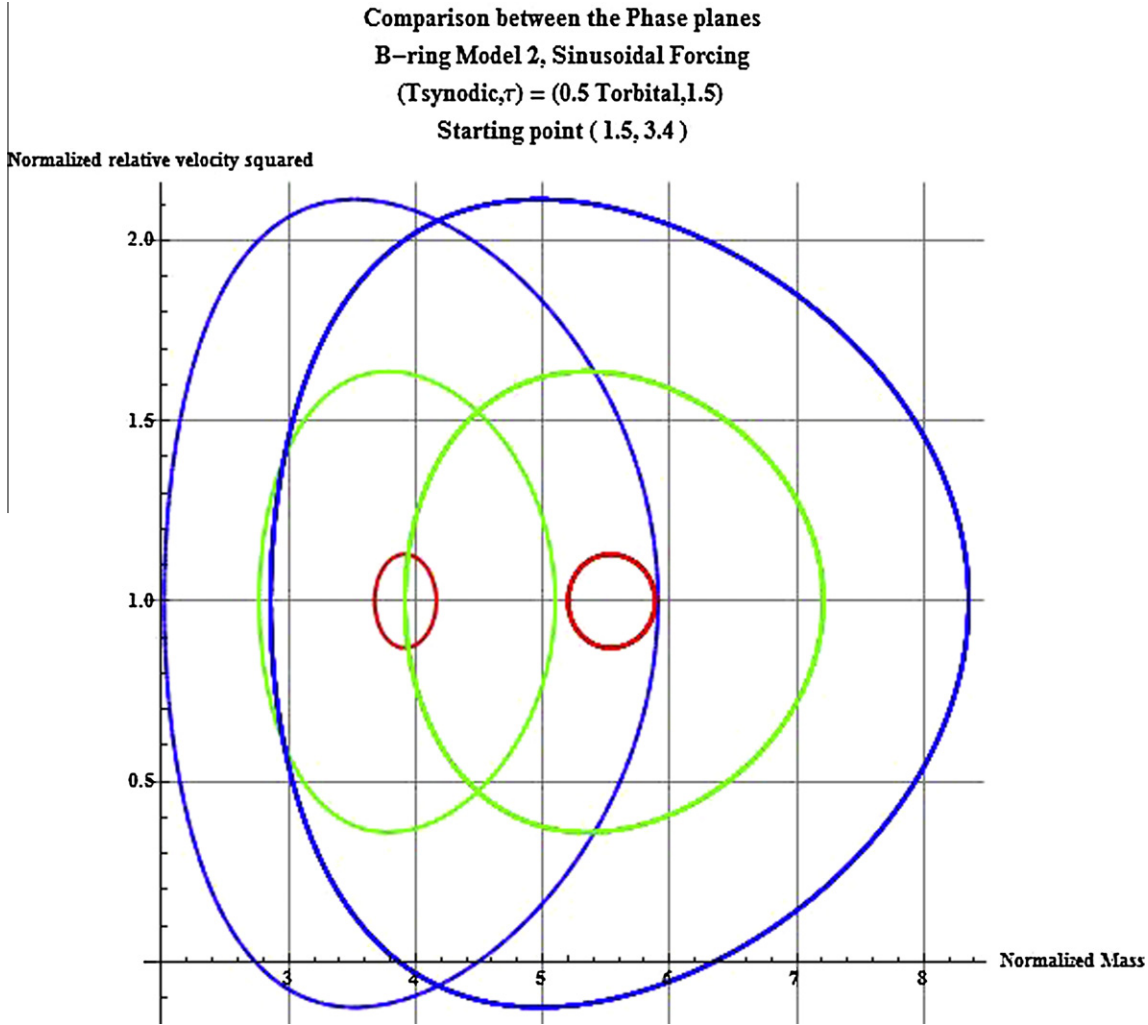


Fig. 16. Phase plane trajectories show the effect of $\tau_{\text{stir}} = 1$ (dashed); 2 (solid) orbital periods. Colors (red, green, blue) show forcing amplitudes $A_0 = 0.1, 0.5, 0.9$ (see Table 1). The excursions are proportional to the forcing amplitude in both cases.

and Lifshitz Volume 1, *Mechanics*, 1960). Figs. 15–17 from our simulations confirm this. The results shown in these figures represent the long-term behavior of the simulated system. They show that the mass maxima lag the v_{rel}^2 minima by $\pi/2$; in the long-term, the system is driven at the forcing period, and both variables are nearly sinusoidal at that forcing period.

10. Speculations and conclusions

Cassini occultations of strongly perturbed locations show strong evidence of clumping. This can be interpreted as aggregation, followed by disaggregation, with timescales of hours to weeks. Disruption may follow from higher-velocity disruptive collisions or tidal shedding of loose pieces (Weidenschilling et al., 1984). Moons may trigger aggregation by streamline crowding (Lewis and Stewart, 2005), which enhances collisions. The evidence from our data shows that these collisions increase structure in the rings rather than destroying it.

We have proposed that in the accretion/disruption balance, collisions initiated by streamline crowding lead to decreased velocity dispersion, and thus increased aggregation. This could allow aggregates to grow from meters to kilometer size, the first step toward accretion of larger objects. However, increased random motions can eventually lead to disruptive collisions, which give the upper hand to fragmentation...just as “irrational exu-

berance” can eventually lead to financial panic in the economy; or the overpopulation of the hares can lead to boom-and-bust in the coupled population of foxes. We conclude that the rings may not have a stable equilibrium for accretion, but instead a boom-and-bust cycle triggered by stochastic events. A small fraction of these events may create more competent objects that are less subject to disruption. Possible mechanisms that could give this result would be collisions compressing the impactors, triggering adhesion (Albers and Spahn, 2006), or simply to bring smaller pieces into contact with larger or higher-density seeds. Those objects could escape the predator–prey cycle, grow and perhaps explain the objects seen in the B ring edge (Spitale and Porco, 2010) and in the F ring (Beurle et al., 2010) near Saturn’s equinox in 2009.

A dense enough aggregate (denser than the critical Roche density $\rho_{\text{crit}} = \frac{3M_p}{4\pi/3a^3}$, for a sphere, see Porco et al., 2007) will tend to act as a seed for further aggregation, as shown in the simulations of Lewis and Stewart (2005). This object will grow until its growth is limited by opening a gap or creating a propeller structure. It will not be disrupted by tidal forces or by collisions with other aggregates, whose relative motions are perturbed by the object’s gravity into non-intersecting trajectories. In the sense of a Markov process, this object has entered an absorbing state (Kemeny and Snell, 1960): it no longer communicates with the other states in the predator–prey system.

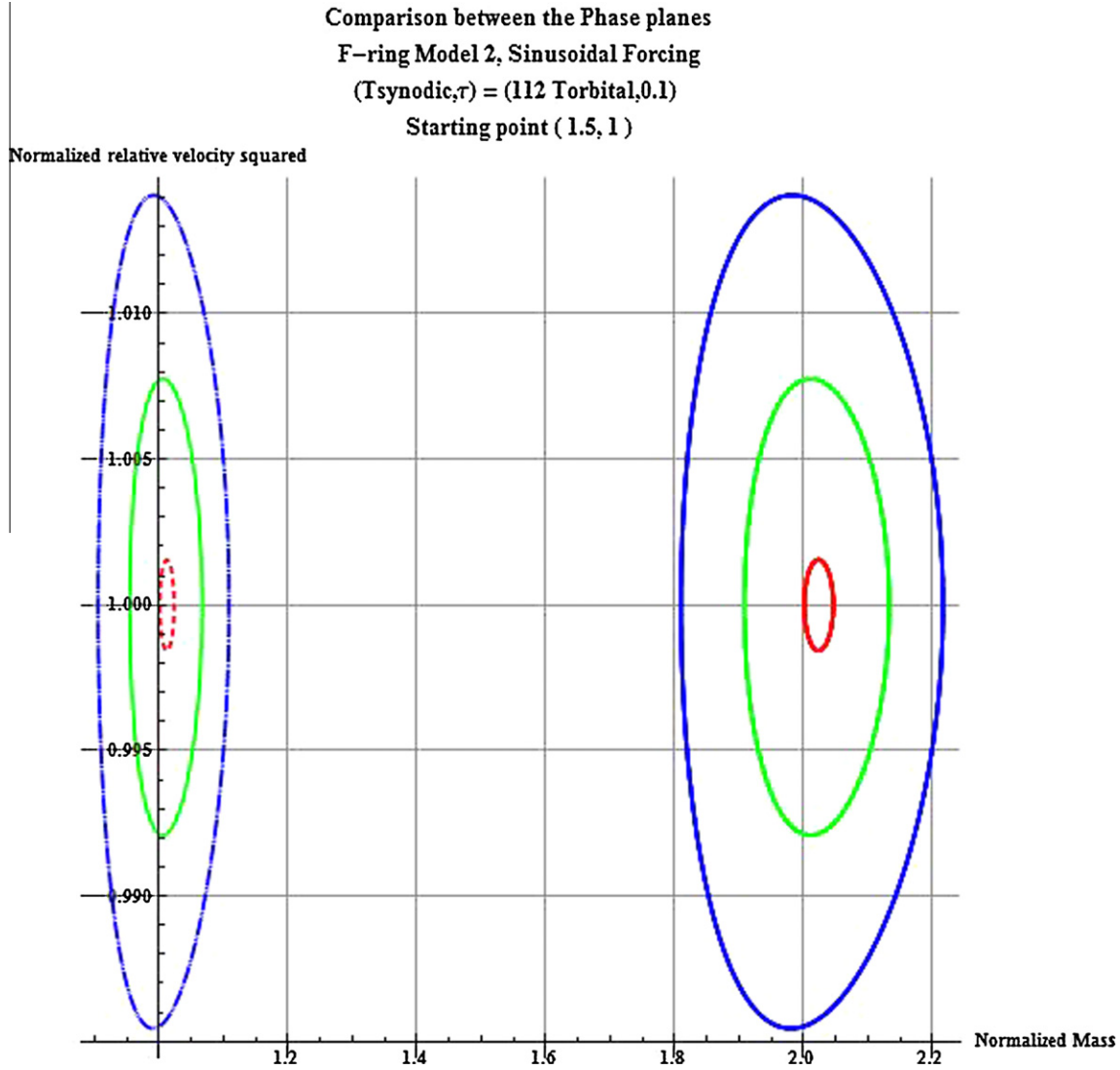


Fig. 17. Same as Fig. 16, except for the F ring. Dashed curves: $\tau_{\text{stir}} = 1$ orbital period. Solid curves: $\tau_{\text{stir}} = 4$ orbital periods. Colors (red, green, blue) show forcing amplitudes $A_0 = 0.1, 0.5, 0.9$ (see Table 1). The excursions are proportional to the forcing amplitudes.

The only way to return the mass in such objects back into the predator–prey system described in this paper is for an external impactor to fragment the moonlet. In the steady state, this will balance the production of such objects (by the hypothesized processes of compaction adhesion, sorting, etc.). Defining the disruption lifetime of a moonlet τ_m , we have in the steady state:

$$\frac{N_{\text{moonlets}}}{T_m} = \alpha \frac{N_{\text{aggregates}}}{T_{\text{coll}}} \quad (16)$$

where N_{moonlets} is number of moonlet bodies, $N_{\text{aggregates}}$ is the number of temporary aggregates, and α is the likelihood of collision between two aggregates that yields a moonlet with $\rho > \rho_{\text{crit}}$.

Taking Meinke et al. (2011) results for moonlets and clumps in Saturn's F ring $\frac{N_{\text{aggregates}}}{N_{\text{moonlets}}} \sim 10$; estimating $T_m \sim 1$ my for a 1 km moonlet (considering the moonlets to be under-dense objects held together mostly by gravity, see Colwell et al. 2000); and $T_{\text{coll}} \sim \frac{T_{\text{orb}}}{4\tau_m}$ (Eq. (6)) with τ_m the optical depth of clumps.

We estimate $\tau_m \sim \frac{N_{\text{aggregates}} R_{\text{aggregates}}}{N_{\text{occ}} \Delta R}$, where N_{occ} is the number of occultations observed by Meinke et al. ($N_{\text{occ}} \sim 100$); $N_{\text{aggregates}}$ is the number of clumps detected by Meinke et al. (2011) ($N_{\text{aggregates}} \sim 20$), $R_{\text{aggregate}}$ is the typical aggregate width (1 km) and ΔR is the radial width of the F ring ($\Delta R \sim 10$ km). This gives

$$\tau_m \sim 0.2 \frac{1 \text{ km}}{10 \text{ km}} \sim 2 \times 10^{-2} \quad (17)$$

and

$$\tau_{\text{coll}} \sim \frac{T_{\text{orb}}}{0.08} \quad (18)$$

and the efficiency of collisions producing moonlets needed to maintain them against disruption by external impactors, from Eq. (16):

$$\alpha \gtrsim \frac{N_{\text{moonlets}}}{N_{\text{aggregates}}} \frac{T_{\text{coll}}}{T_m} \gtrsim \frac{(0.1)}{0.08} \frac{T_{\text{orb}}}{T_m} \gtrsim \frac{T_{\text{orb}}}{1 \text{ my}} = 10^{-9} \quad (19)$$

Thus, if the probability of collision between two aggregates has an efficiency greater than 10^{-9} of creating a seed that grows into a 1 km moonlet, this can balance the disruption rate of such objects by external impacts.

The fortuitous accretion arising from collisions between temporary aggregates provides a natural mechanism for creating solid objects when a shepherd ring edge lies near the Roche limit (see Charnoz et al., 2010; Canup, 2010). As proposed by Charnoz et al., such solid objects can separate from the ring to produce nearby moons. This explains how moons could be born, then move away. If this process continues in Saturn's rings, we would expect solid objects to form at satellite resonances or other perturbed

regions: the B ring edge, the A ring edge, the F ring and similarly perturbed regions near Pan and Daphnis.

Such processes can (1) create the objects seen at the B ring edge and in the F ring in Cassini equinox images, (2) explain the ragged nature of those ring regions and (3) allow for rare events to aggregate ring particles into solid objects, recycling the ring material and extending the ring lifetime.

Acknowledgments

The particular investigations reported here were inspired by Cassini images shown on public web-sites and in Cassini meetings around the time of the Saturn Equinox in 2009. We thank the Cassini imaging team. We thank Ryuji Morishima, Jürgen Schmidt, Frank Spahn, Mark Lewis and Glen Stewart for helpful comments. We thank Mark Showalter and Carl Murray for useful reviews. This research was supported by the Cassini Project and the NASA Cassini Data Analysis Program.

References

- Albers, N., Spahn, F., 2006. The influence of particle adhesion on the stability of agglomerates in Saturn's rings. *Icarus* 181, 292–301.
- Albers, N. et al., 2009. Saturn's F ring as seen by Cassini UVIS: Kinematics and statistics. *Icarus*, submitted for publication.
- Albers, N. et al., 2011. Moon-influenced ringlets and edges in Saturn's rings. Presented at European Geosciences Union, General Assembly, Vienna.
- Baillié, K., Colwell, J.E., Esposito, L.W., Sremcevic, M., 2011. Waves in Cassini UVIS stellar occultations 2. Waves in the C ring. *Icarus* 216, 292–308.
- Barbara, J.M., Esposito, L.W., 2002. Moonlet collisions and the effects of tidally modified accretion in Saturn's F ring. *Icarus* 160, 161–171.
- Beurle, K., Murray, C.D., Williams, G.A., Evans, M.W., Cooper, N.J., Agnor, C.B., 2010. Direct evidence for gravitational instability and moonlet formation in Saturn's rings. *Astrophys. J.* 718, 176–180.
- Bevington, P.R., 1969. *Data Reduction and Error Analysis for the Physical Sciences*. McGraw-Hill, New York.
- Blum, J., 2006. Dust Agglomeration. *Adv. Phys.* 55 (7–8), 881–947.
- Brown, M.B., Forsythe, A.B., 1974. Robust tests for the equality of variances. *J. Amer. Statist. Assoc.*, 364–367.
- Canup, R.M., 2010. Origin of Saturn's rings and inner moons by mass removal from a lost Titan-sized satellite. *Nature*. doi:10.1038/nature09661.
- Canup, R.M., Esposito, L.W., 1995. Accretion in the Roche zone: Coexistence of rings and ringmoons. *Icarus* 113, 331–352.
- Charnoz, S. et al., 2007. The equatorial ridges of Pan and Atlas: Terminal accretionary ornaments? *Science* 318, 1622.
- Charnoz, S., Salmon, J., Crida, A., 2010. The recent formation of Saturn's moonlets from viscous spreading of the main rings. *Nature* 465, 752–754.
- Colwell, J.W., Esposito, L.W., Bundy, D., 2000. Fragmentation rates of small satellites in the outer solar system. *J. Geophys. Res.* 105, 17,589–17,599.
- Colwell, J.E. et al., 2006. Self-gravity wakes in Saturn's A ring measured by stellar occultations from Cassini. *Geophys. Res. Lett.* 33, L07201.
- Colwell, J.E. et al., 2007. Self-gravity wakes and radial structure of Saturn's B ring. *Icarus* 190, 127–144.
- Colwell, J.E. et al., 2009a. Density waves in Cassini UVIS stellar occultations 1. The Cassini division. *Icarus* 200, 574–580.
- Colwell, J.E., Nicholson, P.D., Tiscareno, M.S., Murray, C.D., French, R.G., Marouf, E.A. et al., 2009b. The structure of Saturn's rings. In: Dougherty, M., Esposito, L.W., Krimigis, S.M. (Eds.), *Saturn from Cassini-Huygens*, pp. 375–412.
- Cuzzi, J.N. et al., 2010. An evolving view of Saturn's dynamic rings. *Science* 327, 1470–1475. doi:10.1126/science.1179118.
- Daisaka, H., Tanaka, H., Ida, S., 2001. Viscosity in a dense planetary ring with self-gravitating particles. *Icarus* 154, 296–312.
- Davis, D.R. et al., 1984. Saturn ring particles as dynamic ephemeral bodies. *Science* 224, 744–747.
- Esposito, L.W., 2010. Composition, structure, dynamics and evolution of Saturn's rings. *Ann. Rev. Earth Planet. Sci.* 38, 383–410.
- Esposito, L.W. et al., 1998. Cassini UVIS observations of Saturn's rings. *Planet. Space Sci.* 46, 1221–1235.
- Esposito, L.W. et al., 2004. The Cassini ultraviolet imaging spectrograph investigation. *Space Sci. Rev.* 115, 294–361.
- Esposito, L.W. et al., 2005. Ultraviolet imaging spectroscopy shows an active saturnian system. *Science* 307, 1251–1255.
- Esposito, L.W. et al., 2008. Moonlets and clumps in Saturn's F ring. *Icarus* 194, 278–289.
- Foster, G., 1996. Wavelets for period analysis of unevenly sampled time series. *Astron. J.* 112, 1709–1729.
- Hedman, M.M. et al., 2007. Self-gravity wake structures in Saturn's A ring revealed by Cassini-VIMS. *Astron. J.* 133, 2624–2629.
- Hedman, M.M. et al., 2010. The architecture of the cassini division. *Astron. J.* 139, 228–251. doi:10.1088/0004-6256/139/1/228.
- Hedman, M.M. et al., 2011. The christiansen effect in Saturn's narrow dusty rings and the spectral identification of clumps in the F ring. *Icarus* 215, 695–711.
- Jerousek, R.G., Colwell, J.E., Esposito, L.W., 2011. Morphology and variability of the Titan Ringlet and Huygens Ringlet edges. *Icarus* 216 (1), 280–291.
- Karjalainen, R., Salo, H., 2004. Gravitational accretion of particles in Saturn's rings. *Icarus* 172, 328–348.
- Kemeny, J.G., Snell, J.L., 1960. *Finite Markov Chains*. Van Nostrand, Princeton, NJ.
- Kolvoord et al., 1990. Periodic features in Saturn's F ring: Evidence for nearby moonlets. *Nature* 345, 695–697.
- Koren, I., Feingold, G., 2011. Aerosol-cloud-precipitation system as a predator-prey problem. *PNAS* 108, 12227–12232.
- Lane, A.L. et al., 1982. Photopolarimetry from Voyager 2: Preliminary results on Saturn, Titan, and the rings. *Science* 215, 537–543.
- Lewis, M.C., Stewart, G.R., 2000. Collisional dynamics of perturbed planetary rings. I. *Astron. J.* 120, 3295–3310.
- Lewis, M.C., Stewart, G.R., 2005. Expectations for Cassini observations of ring material with nearby moons. *Icarus* 178, 124–143.
- Lewis, M.C., Stewart, G.R., 2009. Features around embedded moonlets in Saturn's rings: The role of self-gravity and particle size distributions. *Icarus* 199, 387–412.
- Lissauer, J.J., Cuzzi, J.N., 1982. Resonances in Saturn's rings. *Astron. J.* 87, 1051–1058.
- May, R.M., 1974. *Stability and Complexity in Model Ecosystems*, second ed. Princeton University Press, Princeton, NJ.
- Meinke, B.K. et al., 2009. Classification of F ring features observed using Cassini UVIS. In: DPS meeting 41, 22.06. Presented in Puerto Rico, October 2009.
- Meinke, B.K. et al., 2011. Classification of F ring features observed in Cassini UVIS occultations. *Icarus*, submitted for publication.
- Morishima, R., Schmidt, M.W., Stadel, J., 2008. Formation and accretion history of terrestrial planets from runaway growth through to late time: Implications for orbital eccentricity. *Astrophys. J.* 685, 1247–1261.
- Murray, C.D., Dermott, S.F., 1999. *Solar System Dynamics*. Cambridge University Press.
- Murray, C.D. et al., 2005. How Prometheus creates structure in Saturn's F ring. *Nature* 437, 1326–1329.
- Murray, C.D. et al., 2008. The determination of the structure of Saturn's F ring by nearby moonlets. *Nature* 453, 739–744.
- Nicholson, P.D., Hedman, M.M., 2009. Self-gravity wake parameters in Saturn's A and B rings. *Icarus* 206, 410–423.
- Porco, C.C. et al., 2005. Cassini imaging science: Initial results on Saturn's rings and small satellites. *Science* 307 (5713), 1226–1236.
- Porco, C.C. et al., 2007. Saturn's small inner satellites: Clues to their origins. *Science* 318, 1602–1607.
- Scargle, J.D., 1982. Studies in astronomical time series analysis. II – Statistical aspects of spectral analysis of unevenly spaced data. *Astrophys. J.* 263, 835–853.
- Schmidt, J., Ohtsuki, K., Rappaport, N., Salo, H., Spahn, F., 2009. Dynamics of Saturn's dense rings in saturn from cassini-huygens. In: Dougherty, M.K., Esposito, L.W., Krimigis, S.M. (Eds.), *Springer*, pp. 413–458.
- Shu, F.H., Stewart, G.R., 1985. The collisional dynamics of particulate disks. *Icarus* 62, 360–383.
- Spahn, F., Albers, N., Sremcevic, M., Thornton, C., 2004. Kinetic description of coagulation and fragmentation in dilute granular particle ensembles *Europhys. Lett.* 67, 545–551.
- Showalter, M.R., Burns, J.A., 1982. A numerical study of Saturn's F Ring. *Icarus* 52, 526–544.
- Showalter, M.R., Nicholson, P.D., 1990. Saturn's rings through a microscope: Particle size constraints from the Voyager PPS scan. *Icarus* 87, 285–306.
- Spitale, J.N., Porco, C.C., 2010. Detection of free unstable modes and massive bodies in Saturn's outer B ring. 2010. *Astron. J.* 140 (6), 1747–1757.
- Sremčević, M. et al., 2007. A belt of moonlets in Saturn's A ring. *Nature* 449, 1019–1021.
- Sremčević, M. et al., 2008. Density waves in Saturn's rings: Non-linear dispersion and moon libration effects. *Bull. Amer. Astron. Soc.* 40, 430.
- Sremčević, M. et al., 2009. Small-scale ring structure observed in Cassini UVIS occultations. In: DPS meeting 41, 25.03. Presented in Puerto Rico, October 2009.
- Stewart, G.R. et al., 1984. Collision-induced transport processes in planetary rings. In: Greenberg, R., Brahic, A. (Eds.), *Planetary Rings*. Univ. of Arizona Press, Tucson, pp. 447–512.
- Stewart, G.R., Wetherill, G.W., 1988. Evolution of planetesimal velocities. *Icarus* 74, 542–553.
- Tiscareno, M.S. et al., 2006. 100-metre-diameter moonlets in Saturn's A ring from observations of 'propeller' structures. *Nature* 440, 648–650.
- Tiscareno, M.S. et al., 2007. Cassini imaging of Saturn's rings. II. A wavelet technique for analysis of density waves and other radial structure in the rings. *Icarus* 189, 14–34.
- Tiscareno, M.S. et al., 2008. The population of propellers in Saturn's A ring. *Astron. J.* 135, 1083–1091.
- Ward, W.R., Cameron A.G.W., 1978. Disk evolution within the Roche Limit. *Proceedings Lunar Planet Sci Conf IX (Abstract 1205)*.
- Weidenschilling, S.J. et al., 1984. Ring particles—Collisional interactions and physical nature. In: Greenberg, R., Brahic, A. (Eds.), *Planetary Rings*. Univ. of Arizona Press, Tucson, pp. 367–415.